American Mineralogist, Volume 104, pages 857–868, 2019

Estimation of radiation damage in titanites using Raman spectroscopy

Beatrix Muriel Heller[1,*], Nils Keno Lünsdorf[1], István Dunkl[1], Ferenc Molnár[2], and Hilmar von Eynatten[1]

[1]Geoscience Center, Sedimentology and Environmental Geology, University of Göttingen, Goldschmidtstrasse 3, 37077 Göttingen, Germany
[2]Geological Survey of Finland, P.O. Box 96, FI-02151 Espoo, Finland

Abstract

Recent studies have shown that α-damage in titanite influences He diffusivity and thus the closure temperature of the (U-Th)/He system in titanite. We compare different methods for measuring the α-dose in titanite by Raman spectroscopy. Raman spectra of randomly oriented titanite fragments from the Archean Karelian domain in eastern Finland along with some well-studied young titanites and U-Pb standard reference materials were analyzed and related to the concentration of α-emitting elements (U and Th) that generated damage in the respective grains. Automated curve-fitting was performed by the IFORS software and different curve-fitting protocols were tested and compared.

The Raman bands at 424 and 465 cm^{-1} show a good correlation of full-width at half maximum (FWHM) and position with the α-dose. However, these bands are not always present because titanite is highly anisotropic implying that Raman spectra are sensitive to orientation. The intensity-weighted mean FWHM (iw-FWHM) of all Raman bands of a spectrum proves to be the most robust measure of the α-dose. A simplified fitting approach considering 15 peaks is sufficient to describe the accumulated α-dose. For α-doses below 5×10^{16}α/g the iw-FWHM is independent of α-dose and ranges from 25 to 50 cm^{-1}. Above this value the iw-FWHM increases linearly with increasing α-dose up to 3×10^{18}α/g. The linear correlation can be described as iw-FWHM[cm^{-1}] ≈ 39(±1.2)[cm^{-1}] + 3.84(+0.61,–0.26) × 10^{-17}[cm^{-1}/(α/g)] × α-dose[α/g]. The approach provides a pre-selection method to optimize the range of α-doses of titanite crystals to be dated by (U-Th)/He thermochronology.

Keywords: Titanite, (U-Th)/He, metamictization, radiation damage, α-dose, Raman spectroscopy, thermochronology

Introduction

Low-temperature thermochronology is a widely applied tool for deciphering thermal histories of cratonic areas, especially when sedimentary successions constraining the timing of subsidence and exhumation are missing. In contrast to zircon that has commonly effective uranium content (eU = U_{ppm}+0.235Th_{ppm}) of ≥300 ppm (up to 5000 ppm), titanite usually has lower eU contents in the range of 10–500 ppm and is thus less subjected to metamictization. Moreover, titanite is common in intermediate to mafic rocks where zircon is typically absent.

The closure temperature (T_c) of the (U-Th)/He thermochronometers is influenced by the composition and crystalline state of the dated crystals. Among all influencing parameters, metamictization is the dominant one (Flowers 2009; Orme et al. 2016; Johnson et al. 2017). The influence of metamictization on the T_c values of the most widely used minerals, zircon and apatite, has been intensively investigated (Shuster et al. 2006; Flowers et al. 2009; Gautheron et al. 2009; Guenthner et al. 2013; Orme et al. 2016). In contrast, its influence on the titanite (U-Th)/He thermochronometer (THe) has been reported only recently (Baughman et al. 2017; Guenthner et al. 2017). These studies show that with increasing α-dose the T_c of the THe system drops to a significantly lower value. Unfortunately, several aspects of the THe system remain unclear (Reiners and Farley 1999; Stockli and Farley 2004; Cherniak and Watson 2011). Titanite has been discussed as host material for nuclear waste (Weber et al. 1998; Stefanovsky et al. 2004; Lumpkin 2006) and various studies focus on the effects of radiation damage in this mineral (Bismayer et al. 2010; Salje et al. 2011; Beirau et al. 2016).

The α-dose of zircon can be estimated from the width of its main Raman band at approximately 1000–1008 cm^{-1} (Zhang et al. 2000; Nasdala et al. 2001; Palenik et al. 2003; Nasdala et al. 2004). Therefore, Raman spectroscopy offers a quick, non-destructive method for selecting grains for zircon (U-Th)/He (ZHe) thermochronology according to their α-dose (e.g., Ault et al. 2018). For titanite, as for zircon, metamictization affects the Raman spectrum by broadening and shifting the position of several bands (Salje et al. 1993; Meyer et al. 1996; Zhang and Salje 2003; Bismayer et al. 2010; Beirau et al. 2012; Zhang et al. 2013). However, Raman spectroscopy of titanite is more complicated when compared to zircon because of (1) strong anisotropy, (2) higher amount of Raman bands, and (3) adjacent Raman bands often overlap in highly metamict titanite grains (e.g., Beirau et al. 2012; Zhang et al. 2013). Moreover, titanite crystals usually have irregular shapes. Therefore mineral fragments without crystal faces are typically used for THe dating, which makes the crystallographic orientation of the grains difficult.

* Present address: GEOPS, Université Paris-Sud 11, Université Paris-Saclay, Bât. 504, F-91405 Orsay cedex, France. E-mail: b-m.heller@gmx.de

0003-004X/19/0006–857$05.00/DOI: https://doi.org/10.2138/am-2019-6681

So far, no advanced diffusion model exists for titanite that takes radiation damage into consideration. As a consequence, THe ages measured on highly damaged grains are more difficult to interpret than THe ages of slightly damaged grains. Therefore, the routine application of THe thermochronology requires an easy-to-use, orientation independent method for damage estimation and selection of the crystals to be dated.

This study compares different approaches considering single peaks as well as the entire Raman spectrum for quantifying the α-dose in titanite. We present coupled Raman, eU, and THe data of titanite from the Archean Karelian domain in Fennoscandia. The area has been tectonically stable since the Svecofennian orogeny (ca. 1.92–1.80 Ga) (Kähkönen 2005; Lahtinen et al. 2005; Heller et al., in preparation) and since then all samples have experienced the same thermal history. To cover a broad range of α-doses, measurements of younger titanite samples and titanite reference materials with known age and simple cooling histories complement the data set. The main goal of this study is to establish a quick (and non-destructive) method for estimating the α-dose from the titanite Raman spectrum. We demonstrate that characterization of the entire Raman spectrum can be used as a robust estimator independent of grain orientation and evaluation method.

Background

Crystal structure and metamictization of titanite

Titanite, $CaTi(SiO_4)(O,OH,F)$, also called sphene, is a monoclinic nesosilicate. Zig-zag chains of corner-sharing TiO_6 octahedra are cross-linked by isolated SiO_4-tetrahedra, building a framework. This $(TiOSiO_4)_2$-framework contains large cavities that enclose sevenfold-coordinated Ca atoms (Speer and Gibbs 1976). Through lattice substitutions, titanite can incorporate significant amounts of rare earth elements (REE), U, Th, Sr, Y, Mn, and Pb at the sevenfold Ca sites and at the octahedral Ti sites (Higgins and Ribbe 1976; Tiepolo et al. 2002; Xu et al. 2015) and may also concentrate significant amounts of HFSEs, such as Nb, Ta, Zr, and W, on the octahedral Ti site (Groat et al. 1985; Lucassen et al. 2011).

The consecutive radioactive decay of U and Th atoms induces metamictization in titanite crystals (Zhang and Salje 2003; Beirau et al. 2010; Bismayer et al. 2010; Beirau et al. 2012, 2014, 2016; Zhang et al. 2013). In metamict titanites, both crystalline and amorphous domains coexist (Hawthorne et al. 1991; Lumpkin et al. 1991). Hawthorne et al. (1991) and Farges (1997) suggest that metamictization leads to disordering around the Ti positions and a partial reduction of the Ti coordination down to five and/or four. This further disturbs the Ti-O-Ti intra-chain linkages (Beirau et al. 2012), triggering an anisotropic response of the titanite lattice. This means that the plane containing Si-O-Ti-O bond closed contours is less susceptible to a self-accumulation of defects as compared to the perpendicular planes, which contain chains of Ti-O bonds (Beirau et al. 2012).

Raman spectroscopy of titanite

Several studies have applied Raman spectroscopy to titanite (Salje et al. 1993; Meyer et al. 1996; Zhang and Salje 2003; Bismayer et al. 2010; Beirau et al. 2012; Zhang et al. 2013). Titanite is an anisotropic phase, exhibiting Raman spectra strongly dependent on the crystallographic orientation. Up to 40 different Raman bands have been reported for natural titanite samples (Zhang et al. 2013), whereas other authors (Salje et al. 1993) reported only up to 30 bands. The increasing degree of metamictization (Fig. 1) changes the Raman spectrum by broadening bands, shifting their frequency, decreasing the overall intensity and appearance of additional bands (Zhang et al. 2013). As result of metamictization, weakening of the bands at 163, 252, 466, 544, and 605 cm^{-1} (see Fig. 1), appearance of new bands at 574 and 643 cm^{-1}, shifting of bands from 993 to 978 cm^{-1}, 1017 to 1008 cm^{-1}, and 643 to 675 cm^{-1}, and appearance of a shoulder at 650 cm^{-1} have been documented (Zhang et al. 2013).

For estimating the degree of metamictization, Zhang et al. (2013) proposed to use the 605 cm^{-1} peak as it gets broader, shifts toward 612 cm^{-1}, and becomes increasingly asymmetric. Beirau et al. (2012) suggested estimating the degree of metamictization from the full-width at half maximum (FWHM) of the 465 cm^{-1} band, which arises from the SiO_4-bending mode (Heyns et al.

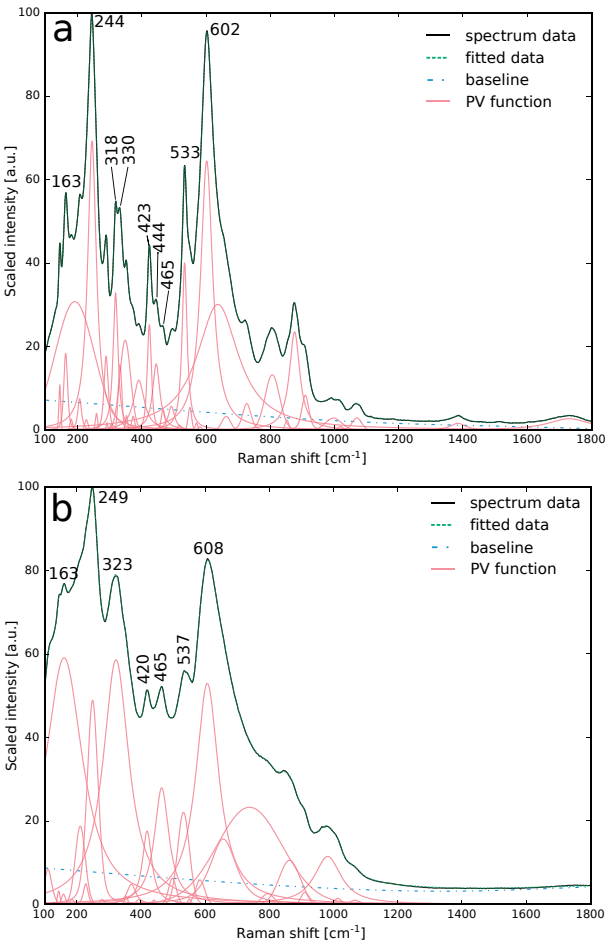

Figure 1. Two Raman spectra of titanite crystals with different α-doses, (**a**) 1.3×10^{13} α/g and (**b**) 1.25×10^{18} α/g. The spectra were evaluated with the software IFORS (Lünsdorf and Lünsdorf 2016). The black lines are the spectrum data, which are mostly covered by the dashed green lines representing fitted data, blue dashed lines are the calculated background correction and thin red lines are the respective pseudo-Voigt functions. The black numbers give the positions of the important bands in cm^{-1}.

2000) and is narrow at low damage doses and broader at high doses. Unfortunately, both approaches can be realized only at given, limited crystallographic orientation and are therefore not useful as a universal method for spectra taken from fragments laying in different orientations.

Importance of radiation damage in (U-Th)/He thermochronology

The radioactive decay of U, Th, and Sm produces α-particles (^{4}He nuclei). Measuring the amount of both ^{4}He and the parent isotopes makes it possible to calculate the duration of He accumulation (Farley 2002; Zeitler 2015).

He has a high diffusivity in solid phases, thus the preserved amount of He in a crystal depends on diffusion that took place in the lifetime of the dated phase. He diffusion kinetics in crystals has been intensely studied; it is controlled by temperature, mineral type, grain size (diffusion domain size), and cooling rate (Zeitler et al. 1987; Wolf et al. 1996). Furthermore, mineral composition and radiation damage are significant (Wolf et al. 1996; Nasdala et al. 2004; Reiners 2005).

Reiners and Farley (1999) have reported grain-size and cooling rate dependence of T_c in the THe system at 165–225 °C. However, recent studies by Baughman et al. (2017) have shown that this is not valid for highly metamict grains. These authors report T_c values of 150–210 °C at low damage levels and a rapid drop above a radiation damage threshold of ~5×10^{17} α/g (for minimal estimates of the temperature where damage accumulation starts, the threshold is ~3.5×10^{17} α/g). Despite the lower threshold of titanite compared to zircon (~1.5×10^{18} α/g; Guenthner et al. 2013; Baughman et al. 2017), titanite is likely to better document the higher temperature portion of a protracted time-temperature path than zircon because of its usually order-of-magnitude lower actinide contents (Baughman et al. 2017).

Samples

The samples used for this study derive from the Ilomantsi greenstone belt, which is located in eastern Finland in the western part of the Neoarchean Karelian province (Fig. 2 and Table 1). It forms part of the Ilomantsi-Kostomuksha greenstone belt, which continues into Russia and extends in a north-south direction over more than 200 km. The Finnish part of this large belt (i.e., Ilomansti greenstone belt, Fig. 2) includes the ~50 long Hattu schist belt, which hosts orogenic gold deposits, and the Kovero belt located further southwest (Nurmi et al. 1993; Sorjonen-Ward 1993; Sorjonen-Ward et al. 2015). The belt is composed of dominantly felsic to intermediate volcanic and siliciclastic rocks with eruption and deposition ages of 2.78–2.75 Ga (Vaasjoki et al. 1993; Huhma et al. 2012b) and small elongated plutons with emplacement ages of ~2.75–2.70 Ga (Vaasjoki et al. 1993; Käpyaho et al. 2016).

The Ilomantsi greenstone belt was affected by two metamorphic events. The Neoarchean metamorphism reached amphibolite facies peak conditions (550 ± 50 °C, 3–5 kbar; O'Brien et al. 1993). An ~2.70 Ga minimum (e.g., cooling) age for this metamorphism was deduced from 2.708 and 2.696 Ga U-Pb ages of titanite and monazite from granodiorite and leucogranite intrusions, respectively (Vaasjoki et al. 1993). However, Hölttä et al. (2016) proposed 2.66 and 2.62 Ga age for the Neoarchean metamorphism based on dating of monazite growth. During the Lapland-Savo orogenic phase of the Paleoproterozoic Svecofennian orogeny, thick, east-verging nappes were emplaced on the Archean basement of eastern Finland and temperatures in the Ilomantsi greenstone belt reached 400–500 °C as indicated by partial reset of hornblende K-Ar ages (Kontinen et al. 1992) and Pb isotope exchange studies (Halla and Heilimo 2009). Biotite K-Ar, as well as biotite and muscovite Ar-Ar ages suggest cooling below ~350–300 °C at ~1.8 Ga (Kontinen et al. 1992; Molnár et al. 2016).

The later orogenies and accretionary events that occurred in Fennoscandia, such as the Gothian (1.64–1.52 Ga) and the Telemarkian accretion (1.52–1.48 Ga), the Hallandian and Danopolonian orogenies (1.47–1.42 Ga), and the Sveconorwegian orogeny (1.14–0.90 Ga) (Bingen et al. 2008) affected mainly the southwestern margin of Fennoscandia and were of little and poorly understood impact for eastern Finland. The lack of sedimentary record makes the reconstruction of the post-Svecofennian thermal evolution difficult (Kohonen 2005).

A kaoline deposit at Virtasalmi, ~200 km WSW of the Ilomantsi greenstone belt, indicates surface exposure of the Svecofennian crystalline basement during the Mesoproterozoic at ~1.18 Ga (Sarapää 1996). Late Neoproterozoic, in Fennoscandia referred to as Vendian, and Cambrian sediments are common further south in Estonia. The extent of this unconformity and sediment coverage toward north (e.g., Finland) is not clear and has been a matter of discussion (Puura et al. 1996; Larson et al. 1999; Sliaupa et al. 2006).

Thermochronologic data from eastern Finland comprise of a wide range of Neoproterozoic and early Paleozoic apatite fission track (AFT) and apatite (U-Th)/He (AHe) ages (Lehtovaara 1976; Lorencak 2003; Murrell 2003; Murrell and Andriessen 2004; Kohn et al. 2009). In combination with new ZHe, THe, and AHe data (Heller et al. in preparation) they indicate that the Ilomantsi greenstone belt experienced slow cooling since the Svecofennian orogeny and that temperatures did not exceed 100 °C for the last 1.0 Ga.

For calculation of radiation damage densities the duration of α-damage accumulation has to be estimated. However, neither the thermal history of the samples in the time interval of 1.8–1.5 Ga (see below) nor the temperature range of α-damage annealing are well defined. While it is a common praxis to estimate that annealing of α-damage occurs at similar temperatures as annealing of fission tracks (Baughman et al. 2017 for titanite and Pidgeon 2014 for zircon), experiments by Gleadow (1978) indicate that α-damage annealing of titanites occurs mainly in the lower part of the titanite fission track partial annealing zone (TPAZ). For the TPAZ different estimates exist (197 °C, Naeser and Forbes 1976; 260 ± 20 °C, Gleadow and Lovering 1978; 250 ± 50 °C, Gleadow and Brooks 1979; 240 ± 40 °C, Harrison et al. 1979; 275 ± 25 °C, Fitzgerald and Gleadow 1988; 275 ± 25 °C, Kohn et al. 1993; 265–310 °C, Coyle and Wagner 1998). Studies including thermal annealing experiments (Bismayer et al. 2010; Beirau et al. 2012; Salje et al. 2012) indicate that α-damage annealing is a complex process occurring over a temperature range; while recovery of point defect is possible at lower temperatures ($T <$ 300 °C), relevant recrystallization of amorphous areas happens only at $T >$ 320 °C. However, note that temperature estimates

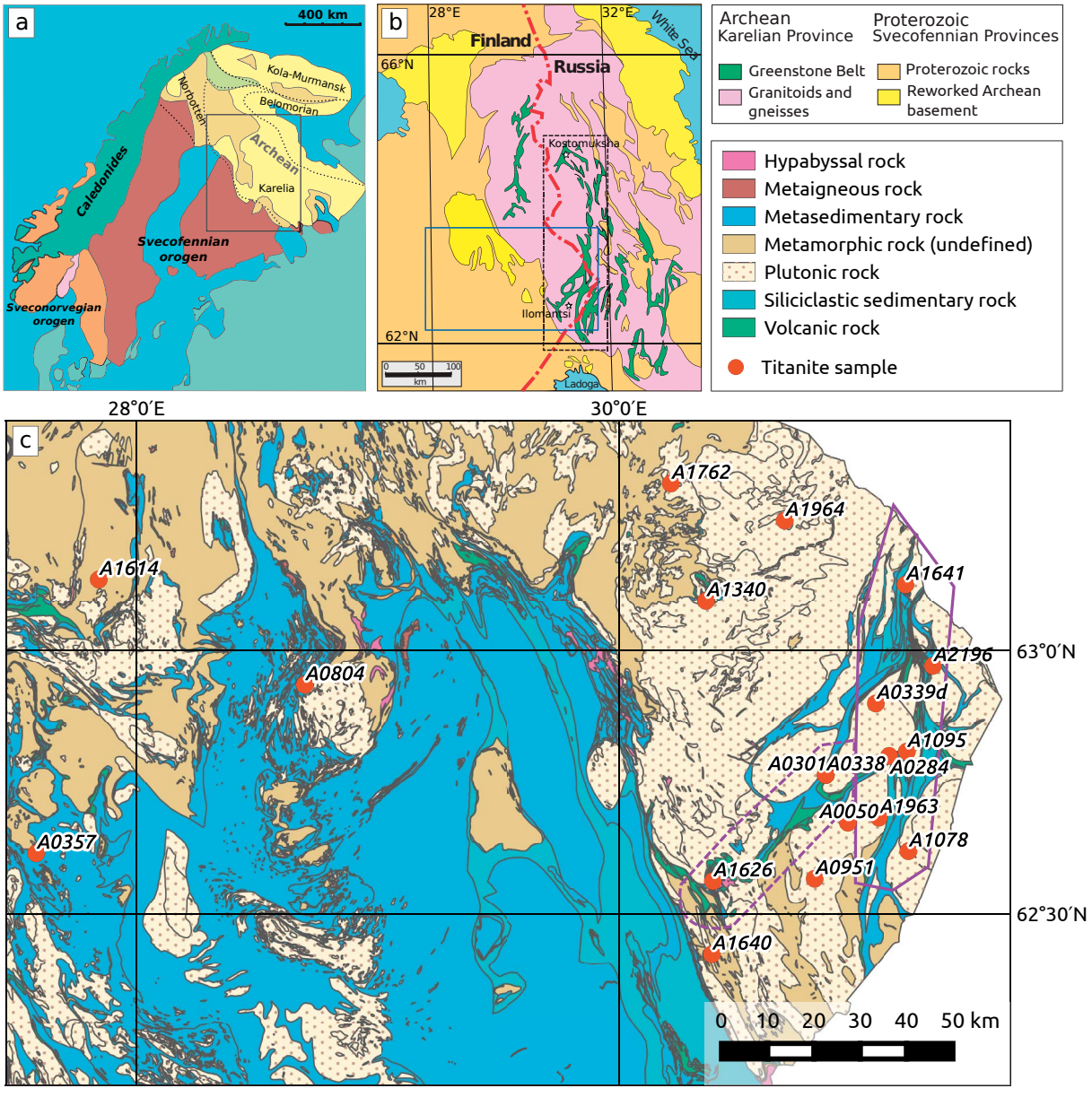

Figure 2. (**a**) Geological overview of Fennoscandia, the black rectangle refers to the area in **b** that shows the entire Ilomantsi-Kostomuksha greenstone belt (black dashed rectangle). The blue rectangle corresponds to the area in **c**. (**c**) Geological map of the Ilomantsi greenstone belt (purple) with the sampling locations (orange circles) in the Karelian domain of Fennoscandia (modified after Koistinen et al. 2001). The Ilomansti greenstone belt consists of the Hattu schist belt (purple polygon) and the Kovero belt (dashed purple polygon).

from thermal annealing experiments are often too high as they do not include geological timescales.

In our case, the onset of α-damage accumulation can be bracketed to 1.5–1.8 Ga. The upper limit is given by the ~1.8 Ga biotite and muscovite K-Ar and Ar-Ar ages (Kontinen et al. 1992; Molnár et al. 2016). Note that Kohn et al. (1993) report that K-Ar ages are always greater or equal to titanite fission track ages. The lower bracket is given by the oldest THe ages (~1.5 Ga) of our samples, which in our case of typical grains sizes and slow cooling correspond to temperatures of ~180 °C.

The time interval from 1.5–1.8 Ga thus corresponds to a temperature drop from ~300 to ~180 °C, the onset of α-damage accumulation lies somewhere in between. Assuming that post-metamorphic cooling was faster in the beginning and then slowed down we decided to calculate with 1.7 Gy as damage accumulation duration. However, due to the uncertainties involved, we also present the results for 1.8, 1.6, and 1.5 Gy accumulation duration and discuss the respective error below.

The sample set with relatively high damage densities from the Ilomantsi belt was complemented by some well-studied titanites (partly reference materials for U-Pb geochronology) of considerably lower α-doses (Table 2).

Table 1. Locality, lithology, and emplacement age of the studied titanite-bearing formations from Finland

Sample	YKJ-north[a]	YKJ-east[a]	Location	Rock type	Zircon U-Pb Age [Ma] (±2s)	Titanite U-Pb Age [Ma] (±2s)	Reference
A0050	6958398	3702479	Ilomantsi	Granodiorite (sanukitoid)	2728 (7)	2707 (10)	Vaasjoki et al. (1993); Heilimo et al. (2011)
A0284	6973076	3710317	Lehtovaara Ilomantsi	Granodiorite	2752 (4)	2705 (10)	Sorjonen-Ward and Claoué-Long (1993); Vaasjoki et al. (1993)
A0301	6968216	3697164	Vehkavaara Ilomantsi	Porphyry (felsic, dike)	2755 (4)	2720 (10)	Vaasjoki et al. (1993); Huhma et al. (2012a)
A0338	6968216	3697164	Vehkavaara Ilomantsi	Porphyry (felsic, dike)		2747 (15)	Vaasjoki et al. (1993)
A0339	6983951	3706826	Silvevaara Ilomantsi	Granodiorite (porphyritic)		2658 (10)	Vaasjoki et al. (1993)
A0357	6945820	3530110	Paukarlahti	Gneiss (granitic, dome)		1824 (10)	Gaal (1980)
A0804	6982475	3586352	Luikonlahti Kaavi	Granite			
A0951	6946074	3696122	Paavonvaara Ilomantsi	Granite			
A1078	6953174	3715702	Oinassalmi Ilomantsi	Diorite (quartz-, sanukitoid)	2744 (3)		Vaasjoki et al. (1993); Heilimo et al. (2011)
A1095	6974229	3713990	Kivisuo Ilomantsi	Porphyry (Qtz-Fldsp)	2756 (6)		Vaasjoki et al. (1993)
A1340	7003399	3669913	Jaakonvaara Lieksa	Diorite	2702 (5)		Halla (2002); Mikkola et al. (2013)
A1614	7003710	3542680	Pajulahti Nilsiä	Syenite			
A1626	6944376	3674468	Rasisuo	Gabbro	2756 (4)		Huhma et al. (2012a)
A1640	6928741	3675065	Huhtilampi	Granite			
A1641	7009265	3711422	Kierrosaho	Granite (microcline)			
A1762	7027497	3661337	Emonvaara	Tonalite		2732 (15)[b]	Huhma et al. (2012b)
A1963	6959880	3708970	Kuikanniemi Ilomantsi	Granodiorite			
A1964	7021049	3685422	Kitsi	Granite			
A2196	6992639	3718302	Viluvaara	Granodiorite	2751 (4)	2737 (15)	Käpyaho et al. (2016)

[a] Finnish national grid.
[b] WR Sm-Nd age.

Methods

Sample preparation

The mineral separation has been performed at the Geological Survey of Finland. The samples were crushed, sieved, and titanite fractions were separated by density and magnetic methods. For single grain analysis, inclusion-free titanite fragments from the 63–200 μm sieve fractions were handpicked. Two to five aliquots of 19 different samples from Finland were chosen. For the polished mineral grain mounts nine Finnish samples as well as six low-damage samples were mounted in epoxy resin disks, ground, and diamond-polished.

Raman spectroscopy

Raman measurements were done on (1) unmounted crystal fragments and (2) polished grain mounts. The measurements were performed with a Horiba XPloRa Plus system equipped with a 532 nm excitation laser (25 mW maximum output power) and an Olympus BX41 microscope, which is coupled to a 200 mm focal length spectrograph with a four-grating turret. The system has a Multi-Pinned-Phase (MPP) open-electrode CCD detector with a precision of ±1 pixel. Using 532 nm the spectral resolution is 1.4 cm^{-1} with the 2400 grooves/mm grating and 2.5 cm^{-1} with the 1800 grooves/mm grating. For the unmounted crystal fragments, the 1800 grooves/mm grating was used and the Raman spectra were collected for 2 × 10 s at 50% laser power with 20× (0.4 NA) or 50× LWD (0.5 NA) objective in 1–3 spots per crystal fragment. The grain mounts were measured with the 2400 grooves/mm grating at 10% laser power with 50× LWD objective. Measurement times were 3 × 5 to 3 × 20 s depending on signal strength.

The positional drift of the spectrometer was checked regularly by measurement of a Si standard and is negligible for this data set. In transparent crystals the penetration depth is about ~15 μm for the 50× LWD objective and ~20 μm for the 20× objective. The theoretical diameters of the Raman spots are ~1.3 μm (50× LWD) and ~1.6 μm (20×).

Spectra were recorded in the range 100–1800 cm^{-1}. For detection of possible photoluminescence bands, additional Raman spectra were taken on some selected grains with a Horiba Jobin-Yvon Labram HR800UV spectrometer equipped with a 633 nm excitation laser. Titanite spectra with a superposed epoxy signal were not used for further evaluation.

Curve-fitting of the Raman spectra

The curve-fitting and spectral evaluation were performed with the IFORS software (Lünsdorf and Lünsdorf 2016). The signal part of the spectrum was modeled by pseudo-Voigt functions (pV functions). In each iteration, a new function was added to the model, and the sum of the squared residuals was reduced by randomly changing a function parameter (e.g., center position, height, width, or shape-factor) by a random value. Two main approaches were applied: (1) using IFORS for background correction and curve-fitting, and (2) manual background correction using the Fityk software (Wojdyr 2010) followed by automated curve-fitting with IFORS.

Table 2. Sources and major parameters of the selected titanite reference samples having low radiation damage densities

Sample	Locality	Source	U-Pb Age [Ma]
ECS	Ecstall pluton, British Columbia	Butler et al. (2002)	91.5
94T	U-Pb reference material; Univ. Arizona	from George Gehrels	51.5
ADA-15	Adamello massif, S. Alps	Schoene et al. (2012)	41.2[a]
LIM	Kaiserstuhl ash, Rhine valley	Kraml et al. (2006)	16.5
MK-221b	Csomád volcano, Carpathians	Molnár (2018)	0.14
MK-5	Csomád volcano, Carpathians	Harangi et al. (2015)	0.03

[a] 20 Ma considered as cooling age and used for α-dose calulation (Heberer et al. 2017).

Reasonable fitting parameters were found by testing different evaluation constraints and visually checking the quality of the fit. The tested parameter values as well as the best configuration setup can be found in Table 3 and Appendix[1] 1.

During the curve-fitting, the spectrum is first scaled to 100 arbitrary intensity units and, in case of automated background correction, the estimated baseline is subtracted in a second step. Thus, the comparison of integrated intensities (by summing the areas of all pV functions) and function areas is only possible in evaluations without automated background correction.

The fitted bandwidths (FWHM, full-width at half maximum) of the titanite spectra were corrected for the apparatus function after Irmer (1985) and Nasdala et al. (2001).

Determination of the concentration of α-emitting elements and the (U-Th)/He ages

Unmounted titanite crystal fragments. For U and Th concentration measurements and (U-Th)/He age determination clear, inclusion-free fragments without external crystal surfaces were hand-picked using a stereo- and a polarizing microscopes. These fragments were photographed and wrapped in platinum capsules with 1 × 1 mm size. The analysis involved three separate steps: (1) He extraction and measurement, (2) chemical digestion, and (3) measurement of the parent isotopes.

For the He measurement, the crystals were degassed in a high vacuum extraction line using an infrared laser. A Ti-Zr getter at 450 °C was used to purify the gas. The inert gases were measured by a Hiden triple-filter quadrupole mass spectrometer with a positive ion-counting detector. For every sample, a re-extraction was done to check the complete degassing of the crystal fragment.

For determination of the mass of U, Th, and Sm, the degassed titanite fragments were dissolved in a mixture of concentrated ultrapure HCl (500 μL) and HF (100 μL) (Reiners and Farley 1999) in pressurized Teflon (polytetrafluoroethylene) vials during one day at 220 °C, and spiked with calibrated ^{230}Th and ^{233}U solutions. After cooling, the samples were dried, converted to nitrate by

TABLE 3. Table of (preliminary) tested values for IFORS automated curve-fitting procedure

Parameter	Tested values	Function of parameter
start_wn	100	Specifies the start wavenumber (Raman shift) of the spectrum
stop_wn	1300, 1800	Specifies the stop wavenumber (Raman shift) of the spectrum
repetitions	1, 3	Sets the number repetitions/determines how often the spectrum is repeatedly evaluated
smoothing	yes, no	If set to "yes", smoothing is enabled and the spectrum will be convoluted with a Hanning-Window filter
smoothing_size	9	Controls the window size of the Hanning-Window used for smoothing
min_width	1, 2	Controls the minimum half-width at half maximum (HWHM) of the pseudo-Voigt functions during curve-fitting
max_width	50, 80, 100, 150	Controls the maximum half-width at half maximum (HWHM) of the pseudo-Voigt functions during curve-fitting
min_distance	2, 5, 8, 10	Controls the minimum distance between two pseudo-Voigt functions during curve-fitting
baseline mode	window_filter, off	Style of baseline approximation. If set to "window_filter", the baseline is approximated by a convolution of the baseline-data with a moving Hanning-window. If set to "off" no baseline will be used during curve-fitting
window_size	0.25, 0.35	Sets the size of the Hanning-window used during baseline approximation when baseline_mode is set to "window_filter"
noise_intensity	1–3.5	This parameter is a multiple of the standard deviation of the estimated noise distribution
max_peak_number	10, 15, 20, 30, 35, 40	Sets the maximum number of pseudo-Voigt functions allowed during curve-fitting, e.g. if this number is reached the program stops
alpha	0.98	During curve-fitting, this parameter controls the width of the normal distribution from which the value is chosen that is added or subtracted from a randomly chosen pseudo-Voigt function parameter
sigma_threshold	0.01, 0.1, 0.5, 1	Controls the duration of the mutation-loop more directly. Legit values for "sigma_threshold" are from the interval "2 > sigma_threshold > 0". Values close to 2 result in short and values close to 0 in long mutation-loop duration

Note: For detailed description of the parameters see Lünsdorf and Lünsdorf (2016), for used curve-fitting protocols see Appendix[1] 1.

re-dissolving in 0.25–1 mL 65% HNO_3 and after a further drying step dissolved in a mixture of 4% HNO_3 with 0.05% HF.

U, Th, Sm, and other REE measurements were performed using a Perkin Elmer Elan DRC II assembled with an APEX MicroFlow nebulizer and a Thermo-iCAP Q ICP-MS instrument. The actinides were determined by isotope dilution technique, while for Ca, Ti, and the other trace elements the external calibration method was applied.

Mounted titanite fragments. The trace element content of titanite grains mounted in polished epoxy resin discs was analyzed by laser ablation ICP-MS. A Resonetics excimer laser was used, coupled to a Thermo-Element 2 sector field mass spectrometer. Measurements were conducted at the same spots as the Raman measurements and performed with 10 μm laser beam diameter and short ablation times. For conversion of the cps data to concentrations, the NIST610 and TNT1500 glass standards were used (Klemme et al. 2008).

RESULTS

Raman spectra

We acquired 82 Raman spectra of 63 unmounted crystal fragments from 19 Finnish samples, as well as 152 spectra of 9 titanite mounts of the Finnish samples and 59 spectra of 6 mounted low-damage samples, totaling 293 titanite Raman spectra.

The Raman spectra show a broad variation in bandwidths, absolute and relative intensities of the bands, as well as shifts in band positions. Figure 1 shows two very different spectra obtained on grains with different α-doses. At the acquisition of the spectra, the crystals were randomly oriented, thus the entire range of anisotropy effects is represented (see e.g., Beirau et al. 2012; Zhang et al. 2013).

Due to the edge-filter, which blocks the signal below ~70 cm^{-1}, most spectra start with signal and many have high Raman intensities at 100–200 cm^{-1}. Therefore, the background signal is detectable only at higher wavenumbers (>1000 cm^{-1}, Fig. 1).

For an excitation wavelength of 532 nm the major photoluminescence bands (Sm, Nd) occur at higher wavenumbers than the titanite Raman bands (Lenz et al. 2015). The comparison of the spectra with spectra acquired with 633 nm excitation shows no differences, which indicates that no REE-related photoluminescence signals overlie the Raman signal. The only photoluminescence that theoretically occurs in the Raman wavenumber range is an Er-generated peak at 564 nm (i.e., = 1060 cm^{-1}), but this has not been detected.

Effective uranium (eU) contents and α-doses

The eU contents of the studied titanite crystal fragments range from 6 to 935 ppm. The α-doses were calculated as:

$$D_{\alpha} = 8 \cdot \frac{C_U \cdot N_A \cdot 0.9928}{M_{238} \cdot 10^6} \cdot \left(\exp^{\lambda 238} \cdot t - 1\right) + 7 \cdot \frac{C_U \cdot N_A \cdot 0.0072}{M_{235} \cdot 10^6} \cdot \left(\exp^{\lambda 235} \cdot t - 1\right) + 6 \cdot \frac{C_{Th} \cdot N_A}{M_{232} \cdot 10^6} \cdot \left(\exp^{\lambda 232} \cdot t - 1\right) \quad (1)$$

where C = actinide concentrations (in parts per million), N_A = Avogadro's number (6.022×10^{23} atoms/mol), M = the molecular masses, λ = the decay constants for the different isotopes, and t = the onset of damage accumulation (t is 1.7 Ga for the Finnish samples as discussed above or the respective ages of the low damage titanites, see Table 2). The α-doses of the Finnish samples range from 4×10^{16} to 2.9×10^{18} α/g and those of the additional samples with lower α-dose from 1.3×10^{13} to 1.8×10^{17}α/g (Appendix[1] 2). Altogether, the α-dose in the samples ranges over more than five orders of magnitude.

Quality of the curve-fitting of the Raman spectra

To establish reasonable curve-fitting parameters and comparison of their effects on further calculations, we applied a systematic sensitivity study and several curve-fitting protocols were tested (Table 3 and Appendix[1] 1). For the completely automated fittings (including automated background correction), reasonable results (setting "wf_sm") were achieved when using a *"window_filter"* parameter with 0.35 window size for baseline calculation, setting the *"noise"* parameter to 2.5 or 3, allowing 40 pV functions and smoothing the spectra with a *"smoothing size"* parameter of 9 (for all other parameter see Appendix[1] 1). Lower *"noise"* parameter values lead to a solution with many small pV functions while higher *"noise"* parameter values or severe restrictions on the maximum number of allowed pV functions either lead to incomplete curve-fits (i.e., some bands

were not described by pV function) or imprecise fitting of broad bands. In most cases, three repeated curve-fits yielded consistent, well-reproducible results. Only a very minor proportion of the spectra showed poor reproducibility.

A problem during curve-fitting of metamict titanite spectra is the inherently unknown background at low wavenumbers. Assuming a flat baseline, even at low wavenumbers seems to be reasonable, however, dispersed light at low wavenumbers might cause some increase in the background intensity. This is why we tested both the automated and manual background correction. The automated curve-fitting often estimates a baseline that is elevated at low wavenumbers (Fig. 1). Too small *"window size"* parameter values (e.g., 0.25) produced unreliable, bended baselines. For manual background correction, a flat baseline (i.e., not elevated at lower wavenumbers) was assumed.

The curve-fitting sometimes produces unapparent solutions; the most common type is when a range in the spectrum is modeled by fitting of one flat, wide pV function and three small narrow pV functions instead of a triplet with three medium-sized functions. The only way to avoid the dubious flat wide pV functions is by limiting the *"maximum peak width"* parameter. Setting the *"maximum peak width"* parameter to 80 or 100 cm^{-1}(given as HWHM, half-width at half maximum) caused fewer artifacts than allowing it to become as high as 150 cm^{-1}. However, harsh restriction of the pV function width (e.g., values below 80 cm^{-1}) is critical because in our case the widths are the most important result of the curve-fitting procedure.

Possibilities of α-dose estimation from the Raman spectra

Single band testing

Beirau et al. (2012) proposed the use of the FWHM of the 465 cm^{-1} band, which is assigned to the SiO_4-bending mode (Heyns et al. 2000; Heyns and Harden 2013), as an estimator for the degree of metamictization because it broadens with increasing α-dose. Figures 3a and 3b show the FWHM of this band (defined by the center values between 458 and 468 cm^{-1}) vs. the α-dose of each spot (Appendix[1] 3). The colors of the data points indicate the band position. In very low damage samples, the band has a width of ~20 cm^{-1} and centers at ~468 cm^{-1}. Above ~5×10^{16}α/g the band starts getting broader and shifts toward lower wavenumbers. However, for highly damaged crystals the bandwidths are very scattered (Fig. 3a) and an accurate estimation becomes difficult. Another problem with the use of this band is its absence in some spectra.

The band at 424 cm^{-1} (415 to 425 cm^{-1}, Figs. 3c and 3d), which is also assigned to the SiO_4-bending mode (Heyns et al. 2000; Heyns and Harden 2013), shows a very similar behavior. Both width and position correlate with the α-dose (Appendix[1] 4). Starting from ~5×10^{16}α/g, band broadening from ~18 to >50 cm^{-1} and positional shift from 424 to 416 cm^{-1} are observed. The 424 cm^{-1} band also does not appear in all spectra.

The bands at 163, 252, 544, and 605 cm^{-1} for which Zhang et al. (2013) report band broadening, as well as the band at 535 cm^{-1} were likewise investigated. However, we could not determine significant correlations. For the bands at 163, 252, and 535 cm^{-1} the bandwidths are scattered and show poor positive correlation with the α-dose while the positions appear to be uncorrelated. For the band at 544 cm^{-1} neither the width nor the position shows any correlation with the α-dose.

According to Zhang et al. (2013) the band at 605 cm^{-1} broadens, shifts toward 612 cm^{-1} and becomes more asymmetric with increasing metamictization. However, Beirau et al. (2012) show that depending on the orientation the band either shifts toward higher wavenumbers or shifts toward lower wavenumbers. Verifying this behavior is hindered by the asymmetric character of the band. Most of the curve-fits contain at least one pV function in the range of 590–620 cm^{-1}, some contain two, rarely three pV functions could be fitted. No correlations with α-dose were observed.

Characterization of the entire Raman spectrum

Metamictization influences some bands more than others but generally it broadens all Raman bands (Zhang et al. 2013). To relate this general broadening with the corresponding α-doses, we looked for parameters that describe the modification of the spectra with a single value. We calculated medians and unweighted and weighted means of all bandwidths for every spectrum. The use of the mean pV function areas was also considered in some test calculations, however, it turns out that the comparison of the function areas is biased in all spectra using automated background correction, because the absolute areas are affected by the baseline height. The use of mean width values instead of single bandwidths has distinct advantages in the case of metamict titanite where the fitting is hampered by overlapping and asymmetric bands.

For the loose grains where two or three spectra were recorded, means and medians combining the two or three spectra were calculated. FWHM means were weighted either by (1) scaled pV function intensity (iw-FWHM) or by (2) scaled pV function area (aw-FWHM). To test the reproducibility, all spectra were curve-fitted three times. Means and medians were calculated for each curve-fit as well as for the average spectrum joining all three evaluations. Usually, the numeric difference between the three repetitions is less than 10% but can be as high as 20% for some spectra (due to overlapping broad bands). Therefore, the use of repeated spectral evaluations and means overall evaluations is highly recommended. The (weighted) means and medians were compared for all tested curve-fitting protocols. All data can be found in Appendix[1] 2.

All means and medians show good correlation with the α-dose (nearly all p-values $<<2.2 \times 10^{-16}$). However, unweighted means and medians are much more sensitive to the curve-fitting parameters and spectral properties (e.g., signal-to-noise ratio) than weighted means. Examples are presented in Appendix[1] 5.

The use of weighted mean FWHM has the advantage that it is less sensitive to the total number of used pV functions and the larger pV functions have a stronger influence than small peaks. Moreover, the weighted mean FWHMs, especially iw-FWHMs, are much more robust because different curve-fitting protocols yield nearly the same results (see Fig. 4).The iw-FWHM yield a better result than the aw-FWHM. The dependency of some bands on the orientation of the crystal seems to have only a minor impact on the iw-FWHM.

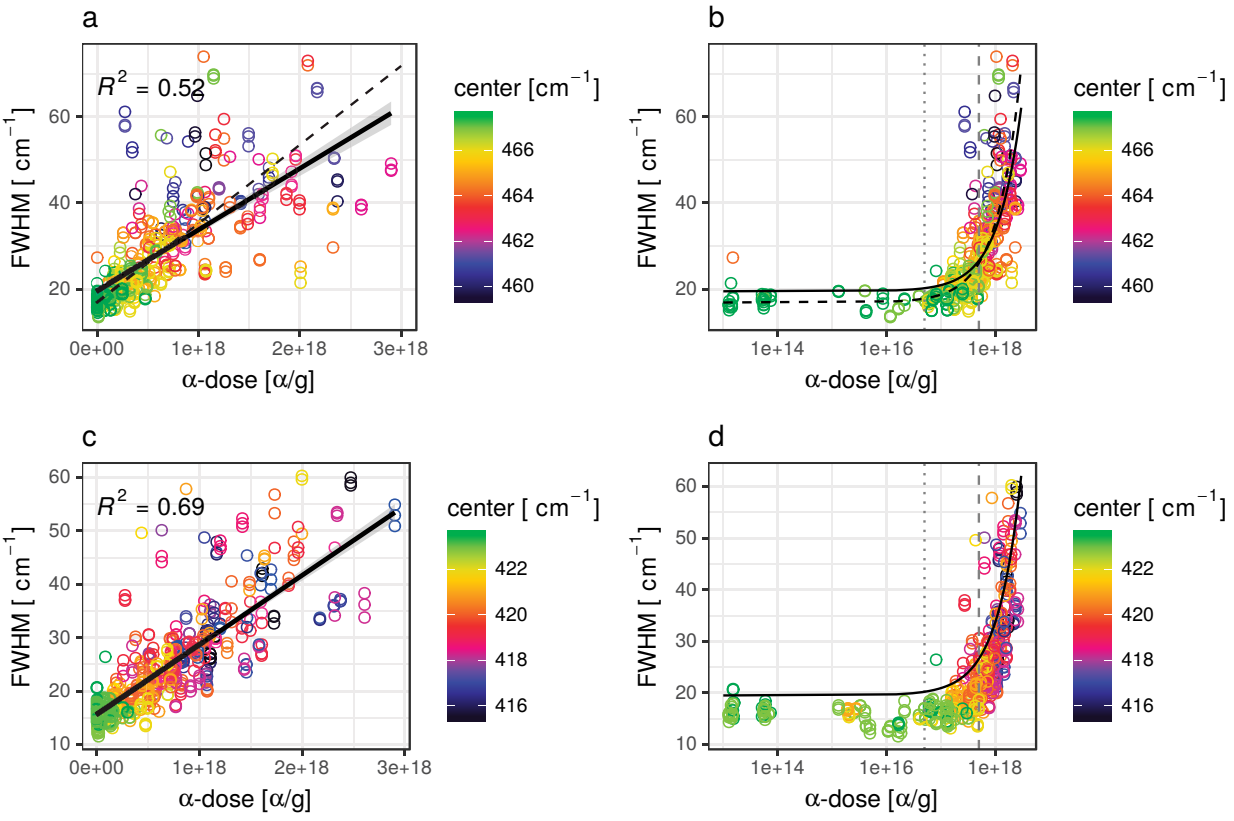

FIGURE 3. α-dose of the analyzed titanite grains vs. the FWHMs of the 465 cm^{-1} band (**a** and **b**) and the 424 cm^{-1} band (**c** and **d**). The linear and logarithmic plots show the same data, but the semi-logarithmic presentation emphasizes better the onset of the significant changes in the crystal lattice—which has prominent importance at helium thermochronology (see in Discussion). The color of the points indicates the position of the center of the pV functions. Only pV functions with an area greater than 1% of the total area and a FWHM < 75 cm^{-1} were considered. Black continuous lines in the linear presentations (**a**) and (**c**) are linear regressions shown with 0.95 confidence intervals (gray belts). Their formulas are FWHM[cm^{-1}] ≈ 19.5(±0.5)[cm^{-1}] + 1.42(±0.06) × 10^{-17}[cm^{-1}/(α/g)] × α-dose[α/g], R^2 = 0.52 for the 465 cm^{-1} band (**a**) and FWHM[cm^{-1}] ≈ 15.6(±0.3)[cm^{-1}] + 1.30(±0.03) × 10^{-17}[cm^{-1}/(α/g)] × α-dose[α/g], R^2 = 0.69 for the 424 cm^{-1} band (**c**). The dashed fit in **a** and **b** with FWHM[cm^{-1}] ≈ 16.9(±0.3)[cm^{-1}] + 1.83(±0.07) × 10^{-17}[cm^{-1}/(α/g)] × α-dose[α/g], R^2 = 0.61 was calculated for all samples with FWHM < 40 cm^{-1} and damage density < 1 × 10^{18} α/g and is more adequate for the low-damage range. The gray dashed vertical lines in **b** and **d** correspond to 5 × 10^{16} α/g and 5 × 10^{17} α/g. For data see Appendices[1] 5 and 6.

The most important sensitivity test: Influence of the maximum number of pV functions on the curve-fitting results

We demonstrated that the iw-FWHM procedure leads to more consistent results than the area-weighted procedure. Thus, a systematic sensitivity test series was performed to study the impact of the maximum number of pV functions on the results of the curve-fitting. The repeated evaluations allowed for 10, 15, 20, 30, or 40 pV functions. Allowing 15 up to 40 pV functions, we always recorded the same trend (see Figs. 4 and 5). However, with only 10 pV functions the spectra were often poorly fitted and especially in the well-crystalline samples not all bands were described by pV functions resulting in higher iw-FWHM values. Thus, curve-fitting with a maximum of 15 pV functions is sufficient to characterize the α-dose in titanites by the iw-FWHM method, even if these 15 pV functions might not represent the spectra in all details.

DISCUSSION

Our results suggest that the intensity weighted mean FWHM is a reliable parameter to describe the α-dose in titanite. The restriction to maximal 15 pV functions led to consistent results. Below an α-dose of 5 × 10^{16} α/g the iw-FWHM is independent of α-dose and scatters between 25 and 50 cm^{-1}. Above this value, the iw-FWHM increases linearly with increasing α-dose up to 3 × 10^{18}α/g.

Figure 5a compares the linear regression parameters (slope, y-axis intercept, and R^2) of all calculated values for all tested curve-fitting protocols. All linear regression data can be found in Appendix[1] 6.The iw-FWHM linear regressions yield the tightest cluster of results associated with high coefficients of determination (Fig. 5a). All the other methods yield more scattered results and especially the median linear regressions often have very low coefficients of determination. This implies that regardless of the curve-fitting protocol used for spectral evaluation, the iw-FWHM method produced nearly the same linear regression, which makes this method the most robust of all tested procedures.

Thus, we recommend using the iw-FWHM as a radiation damage estimator for titanite. For the highest density point in Figure 5a the formula for the linear increase of the iw-FWHM

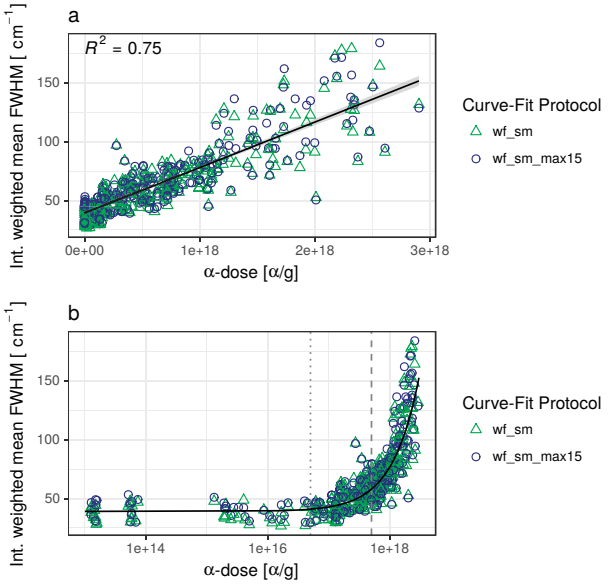

FIGURE 4. Intensity weighted mean FWHMs (iw-FWHM) vs. the α-dose in linear (**a**) and semi-logarithmic (**b**) scale for two curve-fitting protocols, *wf_sm* allowing up to 40 pV functions and *wf_sm_max15* allowing up to 15 pV functions. Black continuous lines correspond to the linear regression calculated over both data sets, shown in **a** with 0.95 confidence interval (gray belt). The formula is iw-FWHM[cm^{-1}] ≈ 39.3(±0.8)[cm^{-1}] + 3.89(±0.09) × 10^{-17}[cm^{-1}/(α/g)] × α-dose[α/g], R^2 = 0.75. The dashed lines indicate the possible threshold values of 5 × 10^{16} α/g (this study) and 5 × 10^{17} α/g (Baughman et al. 2017). Both setups show the same trend that is flat below 5 × 10^{16} α/g and linear above this value. For fitting details see Appendix^1 1.

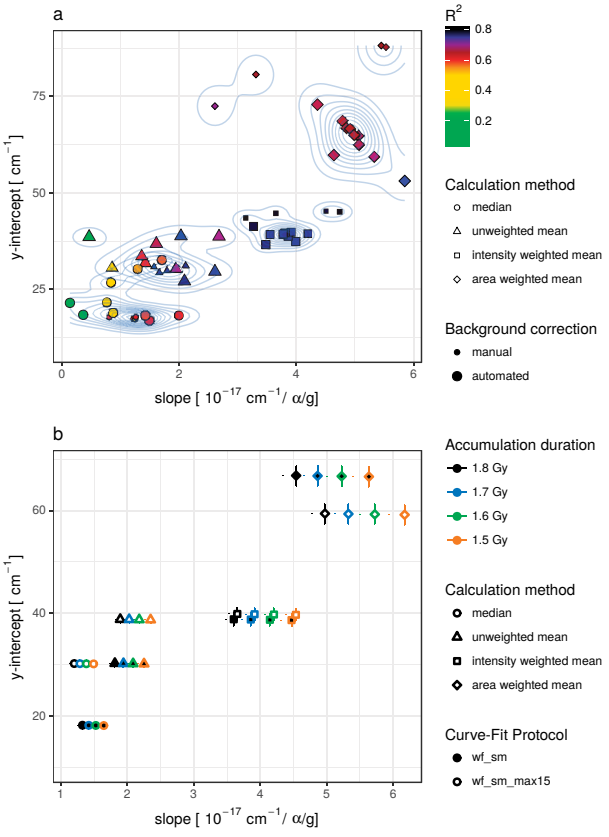

FIGURE 5. (**a**) Summary of the results of the different fitting methods. The axes represent the linear regression parameters of the FWHM vs. α-dose correlations. Symbol shapes refer to calculation method; big symbols are curve-fitting protocols with automated background correction; small symbols are protocols with manual background correction. The color coding gives the coefficient of determination of the linear regressions; the blue lines contour the density distribution. All linear regression parameters for each setting can be found in Appendix^1 5. The generally higher values for weighted means compared to unweighted means and medians are due to the intensity and area weighting. The tightest distribution was generated by the intensity weighted mean FWHMs (iw-FHWM), which yielded very similar results for all different settings, show consistently high R^2 and are thus considered the most robust calculation method. (**b**) shows the linear regression parameters for only two of the curve-fit protocols, *wf_sm* (open symbols) allowing up to 40 pV functions and *wf_sm_max15* (filled symbols) allowing up to 15 pV functions. Linear regressions were calculated for different α-damage accumulation durations that are displayed in different colors. For the intensity weighted mean FWHM the two protocols give very similar results. Lowering the α-damage accumulation duration by 0.1 Gy increases the slope values by ~7–8%.

with growing α-dose is iw-FWHM[cm^{-1}] ≈ 39.2[cm^{-1}] + 3.82 × 10^{-17}[cm^{-1}/(α/g)] × α-dose[α/g]. This is similar to the formula for the most satisfying protocol "wf_sm" (see details in Appendix^1 1), which is iw-FWHM[cm^{-1}] ≈ 38.8(±1.2)[cm^{-1}] + 3.86(±0.13) × 10^{-17}[cm^{-1}/(α/g)] × α-dose[α/g]. Combining both formulas we get iw-FWHM[cm^{-1}] ≈ 39.0(±1.2)[cm^{-1}] + 3.84(±0.13) × 10^{-17}[cm^{-1}/(α/g)] × α-dose[α/g]. The constants of the regression equation are determined by ~3% relative uncertainties.

The other, even more important bias that controls the accuracy of the constants, comes from the assumed duration of the damage accumulation. As discussed above, the temperature range where radiation damage accumulation starts for the Finnish samples is not known precisely, neither is the annealing behavior in titanite. It is not clear how the density of accumulated damage influences the annealing kinetics, and the effect of the variable chemical composition of titanite is not known. Additionally, the thermal history of the Finnish samples bears some uncertainty in the interval of 1.8–1.5 Ga. Figure 5b visualizes the effect of this uncertainty on the linear regressions. While the y-intercepts remain unchanged, shorter damage accumulation durations lead to steeper slopes as the absolute damage gets smaller. This uncertainty is higher than the error derived from the spread of the data. Including this uncertainty into the error of the linear regression leads to a corrected calibration line: iw-FWHM[cm^{-1}] ≈ 39.0(±1.2)[cm^{-1}] + 3.84(+0.61,–0.26) × 10^{-17}[cm^{-1}/(α/g)] × α-dose[α/g].

The onset of the significant change of the titanite Raman peak width is around 5 × 10^{16} α/g. Baughman et al. (2017) studied the He diffusivity and the THe closure temperature in relation to the α-dose. Their data indicate a threshold, where T_c strongly decreases at around ~5 × 10^{17}α/g (Fig. 4). It is remarkable that our procedure based on the characterization of the entire Raman spectrum is more sensitive and detects the

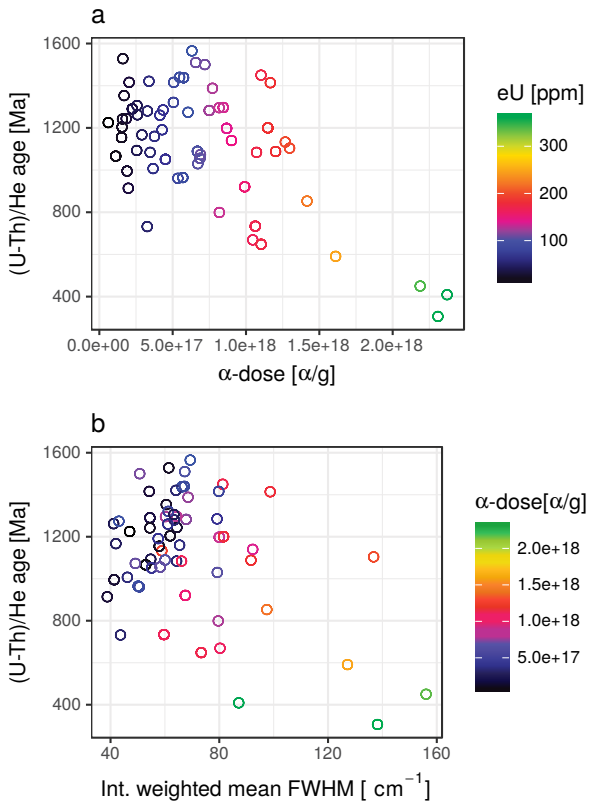

Figure 6. Titanite (U-Th)/He ages in relation to their α-dose, eU contents, and the intensity weighted mean FWHM (iw-FHWM) of the corresponding Raman spectra. (**a**) Titanite (U-Th)/He (THe) ages vs. their α-dose, color indicates the eU contents. (**b**) Relation of the THe ages vs. iw-FHWM. The color indicates the α-dose. The observed dispersion is mainly due to the poor THe age vs. eU correlation of our data set.

change of the lattice at one order of magnitude lower level. This indicates the need for further He diffusion experiments to quantify the diffusion parameters for titanite in the relatively low damage range.

Comparison with (U-Th)/He results

For some of the Finnish samples (U-Th)/He ages were determined. Figure 6a shows these ages compared to their α-dose and eU content. The data show a negative correlation and the covered eU range is relatively small. Compared to our data, the data presented by Baughman et al. (2017) shows a better negative correlation and includes higher eU contents.

Figure 6b shows the THe age vs. the iw-FWHM (fitting with 15 pV functions). As expected, the data show a negative correlation, however,the spread is high. Possible reasons for the dispersion include the moderate correlation of THe age and α-dose, especially at low α-doses, influence of REE on THe ages, α ejection correction (Farley et al. 1996; Stockli and Farley 2004), zoning, and inclusions (the details are discussed in Heller et al. in prep).

Estimation of the α-dose cannot substitute for the THe age determination, however, it enables a pre-selection of the grains most appropriate to target for a specific study.

Implications

We present a robust Raman spectroscopy based method for estimating the α-dose in titanite by Raman spectroscopy. The titanite (U-Th)/He thermochronometer is relevant for the reconstruction of thermal histories in the upper crust, because titanite occurs in more mafic lithologies, in contrast to zircon, and its typically lower actinide content allows for obtaining reliable thermochronologic information in cratonic areas that experienced cooling in Precambrian times. The method can be used in two ways for the routine work in (U-Th)/He thermochronology. (1) It can provide an easy-to-apply and quick tool for identifying highly damaged titanite grains that have extremely low closure temperature due to the high α-dose. In such crystals, the recoil and fission tracks are already in contact and provide a kind of "percolation" leading to very quick helium diffusion (Baughman et al. 2017). Rejecting these titanite grains can optimize the dating procedure by analyzing only the better crystalline grains for which the closure temperature is considerably above the ambient temperature. (2) The other approach is to concentrate on the wide range of the α-doses and aim at involving grains that represent both extremely low and high α-doses to perform a batch modeling (e.g., Orme et al. 2016; Johnson et al. 2017; Hueck et al. 2018). In this way the thermal history may be described with better confidence and even the lower temperature ranges may be better constrained by the titanite grains with very low closure temperature. The method proposed here provides a pre-selection method to optimize the range of α-doses of the dated grains.

Acknowledgments

We thank Hannu Huhma and the Geological Survey of Finland (GTK) for providing the sample material.

References cited

Ault, A.K., Guenthner, W.R., Moser, A.C., Miller, G.H., and Refsnider, K.A. (2018) Zircon grain selection reveals (de)coupled metamictization, radiation damage, and He diffusivity. Chemical Geology, 490, 1–12.

Baughman, J.S., Flowers, R.M., Metcalf, J.R., and Dhansay, T. (2017) Influence of radiation damage on titanite He diffusion kinetics. Geochimica et Cosmochimica Acta, 205, 50–64.

Beirau, T., Bismayer, U., Mihailova, B., Paulmann, C., and Groat, L.A. (2010) Structural phenomena of metamict titanite: a synchrotron, X-ray diffraction and vibrational spectroscopic study. Phase Transitions, 83, 694–702.

Beirau, T., Mihailova, B., Matveeva, G., Kolb, U., Malcherek, T., Groat, L.A., and Bismayer, U. (2012) Structural anisotropy and annealing-induced nanoscale atomic rearrangements in metamict titanite. American Mineralogist, 97, 1354–1365.

Beirau, T., Mihailova, B., Malcherek, T., Paulmann, C., Bismayer, U., and Groat, L.A. (2014) Temperatur-induced *P*21/*c* to *C*2/*c* phase transition in partially amorphous (metamict) titanite revealed by Raman sprectroscopy. Canadian Mineralogist, 52, 91–100.

Beirau, T., Nix, W.D., Ewing, R.C., Schneider, G.A., Groat, L.A., and Bismayer, U. (2016) Mechanical properties of natural radiation-damaged titanite and temperatureinduced structural reorganization: A nanoindentation and Raman spectroscopic study. American Mineralogist, 101, 399–406.

Bingen, B., Andersson, J., Söderlund, U., and Möller, C. (2008) The Mesoproteroic in the Nordic countries. Episodes, 31, 29–34.

Bismayer, U., Paulmann, C., Groat, L., and Zhang, M. (2010) Local phenomena in metamict titanite. Acta Physica Polonica A, 117, 74–77.

Butler, R.F., Gehrels, G.E., Baldwin, S.L., and Davidson, C. (2002) Paleomagnetism and geochronology of the Ecstall pluton in the Coast Mountains of British Columbia: Evidence for local deformation rather than large-scale transport. Journal of Geophysical Research, 107, EPM 3-1–EPM 3-13.

Cherniak, D.J., and Watson, E.B. (2011) Helium diffusion in rutile and titanite, and consideration of the origin and implications of diffusional anisotropy. Chemical Geology, 288, 149–161.

Coyle, D.A., and Wagner, G.A. (1998) Positioning the titanite fission-track partial annealing zone. Chemical Geology, 149, 117–125.

Farges, F. (1997) Fivefold-coordinated Ti^{4+} in metamict zirconolite and titanite:

A new occurrence shown by Ti *K*-edge XANES spectroscopy. American Mineralogist, 82, 44–50.
Farley, K.A. (2002) (U-Th)/He dating: Techniques, calibrations, and applications. Reviews in Mineralogy and Geochemistry, 47, 819–844.
Farley, K.A., Wolf, R.A., and Silver, L.T. (1996) The effects of long alpha-stopping distances on (U-Th)/He ages. Geochimica et Cosmochimica Acta, 60, 4223–4229.
Fitzgerald, P.G., and Gleadow, A.J.W. (1988) Fission-track geochronology, tectonics and structure of the Transantarctic Mountains in northern Victoria Land, Antarctica. Chemical Geology, 73, 1497–1502.
Flowers, R.M. (2009) Exploiting radiation damage control on apatite (U-Th)/He dates in cratonic regions. Earth and Planetary Science Letters, 277, 148–155.
Flowers, R.M., Ketcham, R.A., Shuster, D.L., and Farley, K.A. (2009) Apatite (U-Th)/He thermochronometry using a radiation damage accumulation and annealing model. Geochimica et Cosmochimica Acta, 73, 2347–2365.
Gaal, G. (1980) Geological setting and intrusion tectonics of the Kotalahti nickelcopper deposit, Finland. Bulletin of the Geological Society of Finland, 52, 101–128.
Gautheron, C., Tassan-Got, L., Barbarand, J., and Pagel, M. (2009) Effect of alpha-damage annealing on apatite (U-Th)/He thermochronology. Chemical Geology, 266, 166–179.
Gleadow, A.J.W. (1978) Anisotropic and variable track etching characteristics in natural sphenes. Nuclear Track Detection, 2, 105–117.
Gleadow, A.J.W., and Brooks, C. (1979) Fission-track dating, thermal histories and tectonics of igneous intrusions in east Greenland. Contributions to Mineralogy and Petrology, 71, 45–60.
Gleadow, A.J.W., and Lovering, J.F. (1978) Thermal history of granitic rocks from western Victoria: A fission-track dating study. Journal of the Geological Society of Australia, 25, 323–340.
Groat, L.A., Carter, R.T., Hawthorne, F.C., and Ercit, T.S. (1985) Tantalian niobian titanite from the Irgon claim, southeastern Manitoba. Canadian Mineralogist, 23, 569–571.
Guenthner, W.R., Reiners, P.W., Ketcham, R.A., Nasdala, L., and Giester, G. (2013) Helium diffusion in natural zircon: radiation damage, anisotropy, and the interpretation of zircon (U-TH)/He thermochronology. American Journal of Science, 313, 145–198.
Guenthner, W.R., Reiners, P.W., Drake, H., and Tillberg, M. (2017) Zircon, titanite, and apatite (U-Th)/He ages and age-eU correlations from the Fennoscandian Shield, southern Sweden. Tectonics, 36, 1254–1274.
Halla, J. (2002) Origin and Paleoproterozoic reactivation of Neoarchean high-K granitoid rocks in eastern Finland. Annales Academiae Scientiarum Fennicae, Geologica, Geographica, 163.
Halla, J., and Heilimo, E. (2009) Deformation-induced Pb isotope exchange between K-feldspar and whole rock in Neoarchean granitoids: Implications for assessing Proterozoic imprints. Chemical Geology, 265, 303–312.
Harangi, S., Lukács, R., Schmitt, A.K., Dunkl, I., Molnár, K., Kiss, B., Seghedi, I., Novothny, Á., and Molnár, M. (2015) Constraints on the timing of Quaternary volcanism and duration of magma residence at Ciomadul volcano, east-central Europe, from combined U-Th/He and U-Th zircon geochronology. Journal of Volcanology and Geothermal Research, 301, 66–80.
Harrison, T.M., Armstrong, R.L., Naeser, C.W., and Harakal, J.E. (1979) Geochronology and thermal history of the Coastal Plutonic Complex, near Prince Rupert, British Columbia. Canadian Journal of Earth Sciences, 16, 400–410.
Hawthorne, F.C., Groat, L.A., Raudsepp, M., Ball, N.A., Kimata, M., Spike, F.D., Gaba, R., Halden, N.M., Lumpkin, G.R., Ewing, R.C., et al. (1991) Alpha-decay damage in titanite. American Mineralogist, 76, 370–396.
Heberer, B., Reverman, R.L., Fellin, M.G., Neubauer, F., Dunkl, I., Zattin, M., Seward, D., Genser, J., and Brack, P. (2017) Postcollisional cooling history of the Eastern and Southern Alps and its linkage to Adria indentation. International Journal of Earth Sciences, 106, 1557–1580.
Heilimo, E., Halla, J., and Huhma, H. (2011) Single-grain zircon U-Pb age constraints of the western and eastern sanukitoid zones in the Finnish part of the Karelian Province. Lithos, 121, 87–99.
Heyns, A.M., and Harden, P.M. (2013) The temperature dependence of the Raman spectra of chromium-doped titanite ($CaTiOSiO_4$). Journal of Raman Spectroscopy, 44, 1615–1624.
Heyns, A.M., Harden, P.M., and Prinsloo, L.C. (2000) Resonance Raman study of the high-pressure phase transition in chromium-doped titanite, $CaTiOSiO_4$. Journal of Raman Spectroscopy, 31, 837–841.
Higgins, J.B., and Ribbe, P.H. (1976) Crystal-chemistry and space groups of natural and synthetic titanites. American Mineralogist, 61, 878–888.
Hölttä, P., Lehtonen, E., Lahaye, Y., and Sorjonen-Ward, P. (2016) Metamorphic evolution of the Ilomantsi greenstone belt in the Archaean Karelia Province, eastern Finland. In J. Halla, M.J. Whitehouse, T. Ahmad, and Z. Bagai, Eds., Crust-mantle interactions and granitoid diversification: Insights from Archean Cratons, vol. 449. Special Publications. Geological Society London, London.
Hueck, M., Dunkl, I., Heller, B., Basei, M.A.S., and Siegesmund, S. (2018) (U-Th)/He thermochronology and zircon radiation damage in the South American passive margin: thermal overprint of the Paraná LIP? Tectonics, 37, 1–18.
Huhma, H., Kontinen, A., Mikkola, P., Halkoaho, T., Hokkanen, T., Hölttä, P., Juopperi, H., Konnunaho, J., Luukkonen, E., Mutanen, T., et al. (2012a) Nd isotopic evidence for Archaean crustal growth in Finland. Special Paper of the Geological Survey of Finland, 54, 176–213.
Huhma, H., Mänttäri, I., Peltonen, P., Kontinen, A., Halkoaho, T., Hanski, E., Hokkanen, T., Hölttä, P., Juopperi, H., Konnunaho, J., et al. (2012b) The age of the Archean greenstone belts in Finland. In P. Hölttä, Eds., The Archean of the Karelia Province in Finland, Special Paper 54, pp. 73–174. Geological Survey of Finland.
Irmer, G. (1985) Zum Einfluß der Apparatefunktion auf die Bestimmung von Streuquerschnitten und Lebensdauern aus optischen Phononenspektren. Experimentelle Technik der Physik, 33, 501–506.
Johnson, J.E., Flowers, R.M., Baird, G.B., and Mahan, K.H. (2017) "Inverted" zircon and apatite (U-Th)/He dates from the Front Range, Colorado: High damage zircon as a low-temperature (<50°C) thermochronometer. Earth and Planetary Science Letters, 466, 80–90.
Kähkönen, Y. (2005) Svecofennian supracrustal rocks. In M. Lehtinen, P.A. Nurmi and O.T. Rämö, Eds., Precambrian Geology of Finland—Key to the evolution of the Fennoscandian shield. Developments in Precambrian Geology 14, chapter 8, p. 343–405. Elsevier.
Käpyaho, A., Molnár, F., Sorjonen-Ward, P., Mänttäri, I., Sakellaris, G., and Whitehouse, M. (2016) New U-Pb age constraints for the timing of gold mineralization at the Pampalo gold deposit, Archaean Hattu schist belt, eastern Finland, obtained from hydrothermally altered and recrystallised zircon. Precambrian Research, 289, 48–61.
Klemme, S., Prowatke, S., Münker, C., Magee, C., Lahaye, Y., Zack, T., Kasemann, S., Cabato, E., and Kaeser, B. (2008) Synthesis and preliminary characterization of new silicate, phosphate and titanite reference glasses. Geostandards and Geoanalytical Research, 32, 39–54.
Kohn, B.P., Lorencak, M., Gleadow, A.J.W., Kohlmann, F., Raza, A., Osadetz, K.G., and Sorjonen-Ward, P. (2009) A reappraisal of low-temperature thermochronology of the eastern Fennoscandia Shield and radiation-enhanced apatite fission-track annealing. Geological Society, London, Special Publications, 324, 193–216.
Kohn, B.P., Wagner, M.E., Lutz, T.M., and Organist, G. (1993) Anomalous Mesozoic thermal regime, central Appalachian Piedmont: evidence from sphene and zircon fission-track dating. Journal of Geology, 101, 779–794.
Kohonen, J. (2005) Sedimentary rocks, diabases, and late cratonic evolution. In M. Lehtinen, P.A. Nurmi, and O.T. Rämö, Eds., Precambrian geology of Finland—Key to the evolution of the Fennoscandian shield. Developments in Precambrian Geology 14, chapter 13, p. 563–603. Elsevier.
Koistinen, T., Stephens, M.B., Bogatchev, V., Nordgulen, Ø., Wennerstrøm, M., and Korhonen, J. (2001) Geological map of the Fennoscandian Shield, scale 1:2 million. Geological Surveys of Finland, Norway and Sweden and North-West Department of Natural Resources of Russia.
Kontinen, A., Paavola, J., and Lukkarinen, H. (1992) K-Ar ages of hornblende and biotite from late Archaean rocks of eastern Finland—interpretation and discussion of tectonic implications. Geological Survey of Finland, Bulletin, 365, 1–31.
Kraml, M., Pik, R., Rahn, M., Selbekk, R., Carignan, J., and Keller, J. (2006) A new multi-mineral age reference material for $^{40}Ar/^{39}Ar$, (U-Th)/He and fission track dating methods: The Limberg t3 Tuff. Geostandards and Geoanalytical Research, 30, 73–86.
Lahtinen, R., Korja, A., and Nironen, M. (2005) Paleoproterozoic tectonic evolution. In M. Lehtinen, P.A. Nurmi, and O.T. Rämö, Eds., Precambrian geology of Finland—Key to the evolution of the Fennoscandian shield. Developments in Precambrian Geology 14, chapter 11, p. 481–531. Elsevier.
Larson, S.Å., Tullborg, E.L., Cederbom, C., and Stiberg, J.P. (1999) Sveconorwegian and Caledonian foreland basins in the Baltic Shield revealed by fission-track thermochronology. Terra Nova, 11, 210–215.
Lehtovaara, J. (1976) Apatite fission track dating of Finnish Precambrian intrusives. Annales Academiae Scientiarum Fennicae, 117, 1–94.
Lenz, C., Nasdala, L., Talla, D., Hauzenberger, C., Seitz, R., and Kolitsch, U. (2015) Laser-induced REE^{3+} photoluminescence of selected accessory minerals—An "advantageous artefact" in Raman spectroscopy. Chemical Geology, 415, 1–16.
Lorencak, M. (2003) Low temperature thermochronology of the Canadian and Fennoscandian Shields, 300 p. Ph.D. thesis, University of Melbourne.
Lucassen, F., Franz, G., Dulski, P., Romer, R.L., and Rhede, D. (2011) Element and Sr isotope signatures of titanite as indicator of variable fluid composition in hydrated eclogite. Lithos, 121, 12–24.
Lumpkin, G.R. (2006) Ceramic waste forms for actinides. Elements, 2, 365–372.
Lumpkin, G.R., Eby, R.K., and Ewing, R.C. (1991) Alpha-recoil damage in titanite ($CaTiSiO_5$): direct observation and annealing study using high resolution transmission electron microscopy. Journal of Materials Research, 6, 560–564.
Lünsdorf, N.K., and Lünsdorf, J.O. (2016) Evaluating Raman spectra of carbonaceous matter by automated, iterative curve-fitting. International Journal of Coal Geology, 160–161, 51–62.
Meyer, H.W., Zhang, M., Bismayer, U., Salje, E.K.H., Schmidt, C., Kek, S., Morgenroth, W., and Bleser, T. (1996) Phase transformation of natural titanite: An

infrared, Raman spectroscopic, optical birefringence and X-ray diffraction study. Phase Transitions, 59, 39–60.
Mikkola, P., Heilimo, E., Paavola, J., Halkoaho, T., Äikäs, O., and Huhma, H. (2013) Lentuan kompleksin eteläosan kallioperä. Summary: Bedrock of the southern part of the Lentua complex. Tutkimusraportti—Report of Investigation, 202, 96.
Molnár, K. (2018) Eruption chronology of the Ciomadul volcanic complex based on zircon (U-Th)/He geochronology. Unpublished Ph.D. thesis, Eötvös University, Budapest.
Molnár, F., O'Brien, H., Lahaye, Y., Kapyaho, A., and Sakellaris, G. (2016) Signatures of Multiple Mineralization Processes in the Archean Orogenic Gold Deposit of the Pampalo Mine, Hattu Schist Belt, Eastern Finland. Economic Geology, 111, 1659–1703.
Murrell, G.R. (2003) The long-term thermal evolution of central Fennoscandia, revealed by low-temperature thermochronometry, 219 p. Ph.D. thesis, Vrije Universiteit Amsterdam.
Murrell, G.R., and Andriessen, P.A.M. (2004) Unravelling a long-term multi-event thermal record in the cratonic interior of southern Finland through apatite fission track thermochronology. Physics and Chemistry of the Earth, 29, 695–706.
Naeser, C.W., and Forbes, R.B. (1976) Variation of fission track ages with depth in two deep drill holes. Eos, Transactions American Geophysical Union, 57, 353.
Nasdala, L., Wenzel, M., Vavra, G., Irmer, G., Wenzel, T., and Kober, B. (2001) Metamictisation of natural zircon: accumulation versus thermal annealing of radioactivity-induced damage. Contributions to Mineralogy and Petrology, 141, 125–144.
Nasdala, L., Reiners, P.W., Garver, J.I., Kennedy, A.K., Stern, R.A., Balan, E., and Wirth, R. (2004) Incomplete retention of radiation damage in zircon from Sri Lanka. American Mineralogist, 89, 219–231.
Nurmi, P.A., Sorjonen-Ward, P., and Damstén, M. (1993) Geological setting, characteristics and exploration history of the mesothermal gold ocurrences in the late Archean Hattu schist belt, Ilomantsi, eastern Finland. In P. Nurmi and P. Sorjonen-Ward, Eds., Geological Development, Gold Mineralization and Exploration Methods in the Late Archean Hattu Schist Belt, Ilomantsi, Eastern Finland, Special Paper 17, Geological Survey of Finland, Espoo, pp. 193–231.
O'Brien, H., Huhma, H., and Sorjonen-Ward, P. (1993) Petrogenesis of the Late Archean Hattu schist belt, Ilomantsi, eastern Finland: Geochemistry and Sr, Nd isotopic composition. In P.A. Nurmi and P. Sorjonen-Ward, Eds., Geological Development, Gold Mineralization and Exploration Methods in the Late Archean Hattu Schist Belt, Ilomantsi, Eastern Finland, Special Paper 17, Geological Survey of Finland, Espoo, pp. 147–184.
Orme, D.A., Guenthner, W.R., Laskowski, A.K., and Reiners, P.W. (2016) Longterm tectonothermal history of Laramide basement from zircon-He age-eU correlations. Earth and Planetary Science Letters, 453, 119–130.
Palenik, C.S., Nasdala, L., and Ewing, R.C. (2003) Radiation damage in zircon. American Mineralogist, 88, 770–781.
Pidgeon, R.T. (2014) Zircon radiation damage ages. Chemical Geology, 367, 13–22.
Puura, V., Amantov, A., Tikhomirov, S., and Laitakari, I. (1996) Latest events affecting the Precambrian basement, Gulf of Finland and surrounding areas. Special Paper of the Geological Survey of Finland, 21, 115–125.
Reiners, P.W. (2005) Zircon (U-Th)/He thermochronometry. Reviews in Mineralogy and Geochemistry, 58, 151–179.
Reiners, P.W., and Farley, K.A. (1999) Helium diffusion and (U-Th)/He thermochronometry of titanite. Geochimica et Cosmochimica Acta, 63, 3845–3859.
Salje, E.K.H., Schmidt, C., and Bismayer, U. (1993) Structural phase transition in titanite, $CaTiSiO_5$: A ramanspectroscopic study. Physics and Chemistry of Minerals, 19, 502–506.
Salje, E.K., Safarik, D.J., Lashley, J.C., Groat, L.A., and Bismayer, U. (2011) Elastic softening of metamict titanite $CaTiSiO_5$: Radiation damage and annealing. American Mineralogist, 96, 1254–1261.
Salje, E.K.H., Taylor, R.D., Safarik, D.J., Lashley, J.C., Groat, L.A., Bismayer, U., Evans, J.R., and Friedman, R. (2012) Evidence for direct impact damage in metamict titanite $CaTiSiO_5$. Journal of Physics: Condensed Matter, 24, 052202.
Sarapää, O. (1996) Proterozoic primary kaolin deposits at Virtasalmi, south-eastern Finland. Ph.D. thesis, University of Helsinki, 169 p.
Schoene, B., Schaltegger, U., Brack, P., Latkoczy, C., Stracke, A., and Günther, D. (2012) Rates of magma differentiation and emplacement in a ballooning pluton recorded by U-Pb TIMS-TEA, Adamello batholith, Italy. Earth and Planetary Science Letters, 355-356, 162–173.
Shuster, D.L., Flowers, R.M., and Farley, K.A. (2006) The influence of natural radiation damage on helium diffusion kinetics in apatite. Earth and Planetary Science Letters, 249, 148–161.
Sliaupa, S., Fokin, P.A., Lazauskiene, J., and Stephenson, R.A. (2006) The Vendian-Early Palaeozoic sedimentary basins of the East European Craton. In D.G. Gee and R.A. Stephenson, Eds., European Lithosphere Dynamics, 32, p. 449–462. Memoirs. Geological Society London, London.
Sorjonen-Ward, P. (1993) An overview of structural evolution and lithic units within and intruding the late Archean Hattu schist belt, Ilomantsi, eastern Finland. In P.A. Nurmi and P. Sorjonen-Ward, Eds., Geological development, gold mineralization and exploration methods in the late Archean Hattu schist belt, Ilomantsi, eastern Finland. Special Paper 17, p. 9–102. Geological Survey of Finland, Espoo.
Sorjonen-Ward, P., and Claoué-Long, J. (1993) A preliminary note on ion probe results for zircons from the Silvevaara Granodiorite, Ilomantsi, eastern Finland. In S. Autio, Ed., Geological Survey of Finland, Current Research 1991–1992. Special Paper 18. Geological Survey of Finland, pp. 25–29.
Sorjonen-Ward, P., Hartikainen, A., Nurmi, P., Rasilainen, K., Schaubs, P., Zhang, Y., and Liikanen, J. (2015) Exploration Targeting and Geological Context of Gold Mineralization in the Neoarchean Ilomantsi Greenstone Belt in Eastern Finland. In W.D. Maier, R. Lahtinen, and H. O'Brien, Eds., Mineral Deposits of Finland, chapter 5.3, p. 435–466. Elsevier.
Speer, J.A., and Gibbs, G.V. (1976) The crystal structure of synthetic titanite, $CaTiOSiO_4$, and the domain textures of natural titanites. American Mineralogist, 61, 238–247.
Stefanovsky, S.V., Yudintsev, S.V., Giere, R., and Lumpkin, G.R. (2004) Nuclear waste forms. In R. Gierié and P. Stille, Eds., Energy, Waste and the Environment: a Geochemical Perspective. Special Publications 236. Geological Society London, pp. 37–63.
Stockli, D.F., and Farley, K.A. (2004) Empirical constraints on the titanite (UTh)/ He partial retention zone from the KTB drill hole. Chemical Geology, 207, 223–236.
Tiepolo, M., Oberti, R., and Vannucci, R. (2002) Trace-element incorporation in titanite: Constraints from experimentally determined solid/liquid partition coefficients. Chemical Geology, 191, 105–119.
Vaasjoki, M., Sorjonen-Ward, P., and Lavikainen, S. (1993) U-Pb age determinations and sulfide Pb-Pb characteristics from the late Archean Hattu schist belt, Ilomantsi, eastern Finland. In P.A. Nurmi and P. Sorjonen-Ward, Eds., Geological Development, Gold Mineralization and Exploration Methods in the Late Archean Hattu Schist Belt, Ilomantsi, Eastern Finland. Special Paper 17. Geological Survey of Finland, Espoo, pp. 103–131.
Weber, W.J., Ewing, R.C., Catlow, C.R.A., Hobbs, L.W., Kinoshita, C., Motta, A.T., Nastasi, M., and Salje, E.K.H. (1998) Radiation effects in crystalline ceramics for the immobilization of high-level nuclear waste and plutonium. Journal of Materials Research, 13.
Wojdyr, M. (2010) Fityk: a general-purpose peak fitting program. Journal of Applied Crystallography, 43, 1126–1128.
Wolf, R.A., Farley, K.A., and Silver, L.T. (1996) Helium diffusion and low-temperature thermochronometry. Planetary Sciences, 60, 4231–4240.
Xu, L., Bi, X., Hu, R., Tang, Y., Wang, X., and Xu, Y. (2015) LA-ICP-MS mineral chemistry of titanite and the geological implications for exploration of porphyry Cu deposits in the Jinshajiang—Red River alkaline igneous belt, SW China. Mineralogy and Petrology, 109, 181–200.
Zeitler, P.K. (2015) U-Th/He dating. In J.W. Rink and J.W. Thompson, Eds., Encyclopedia of Scientific Dating Methods, pp. 932–940. Springer.
Zeitler, P.K., Herczeg, A.L., McDougall, I., and Honda, M. (1987) U-Th-He dating of apatite: A potential thermochronometer. Geochimica et Cosmochimica Acta, 51, 2865–2868.
Zhang, M., and Salje, E.K.H. (2003) Spectroscopic characterization of metamictization and recrystallization in zircon and titanite. Phase Transitions, 76, 117–136.
Zhang, M., Salje, E.K.H., Farnan, I., Graeme-Barber, A., Daniel, P., Ewing, R.C., Clark, A.M., and Leroux, H. (2000) Metamictization of zircon: Raman spectroscopic study. Journal of Physics: Condensed Matter, 12, 1915–1925.
Zhang, M., Salje, E.K.H., Redfern, S.A.T., Bismayer, U., and Groat, L.A. (2013) Intermediate structures in radiation damaged titanite ($CaTiSiO_5$): a Raman spectroscopic study. Journal of Physics: Condensed Matter, 25, 12.

Manuscript received June 13, 2018
Manuscript accepted February 18, 2019
Manuscript handled by Yann Morizet

Endnote:

[1]Deposit item AM-19-66681, Supplemental Appendices. Deposit items are free to all readers and found on the MSA website, via the specific issue's Table of Contents (go to http://www.minsocam.org/MSA/AmMin/TOC/2019/Jun2019_data/Jun2019_data.html).